Heliyon 9 (2023) e18875

Contents lists available at ScienceDirect

Heliyon

journal homepage: www.cell.com/heliyon

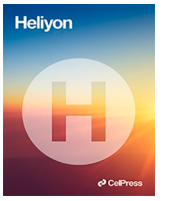

Response characteristics of $MAPbBr_3$ direct conversion X-ray detectors based on measurements and Monte Carlo simulation

Feng Qin [a,b], Rui Zhao [b], Wei Feng Zhu [b,c], Ning Qin Deng [b], Zhi Wei Jiao [a], Xian Qiang Tang [b,c], Jin Jie Wu [b,*]

[a] China Jiliang University, Hangzhou, 310018, China
[b] National Institute of Metrology, Beijing, 100029, China
[c] Chengdu University of Technology, Chengdu, 610059, China

ARTICLE INFO

Keywords:
Direct conversion X-ray detectors
Low energy X-ray
Absorption efficiency
Detection sensitivity

ABSTRACT

In recent years, higher requirements have been placed on the response characteristics of X-ray detectors in the field of medical diagnostic imaging. Due to this, high sensitivity, high attenuation coefficient and low cost detection materials need to be developed. In this paper, the geometric model of a detector was established by Geant4 code. The absorption efficiency and mass attenuation coefficient of $MAPbBr_3$ crystals were calculated in the energy range of 30 keV to 100 keV. Compared with the mass attenuation coefficient of the NIST database, the deviation was within 1.39%. The signal charge number and detection sensitivity of the X-ray interaction with the $MAPbBr_3$ crystal ware calculated. Compared with the CdTe crystal and α-Se, the $MAPbBr_3$ crystal still had a larger detection sensitivity under a smaller applied electric field, which was approximately 9 times higher than that of α-Se. This result indicated that the detection sensitivity could be greatly improved by using a high atomic number and high charge mobility-lifetime product. Based on the simulation results, the 2 mm thick $MAPbBr_3$ crystal exhibited the highest detection sensitivity at 60 keV X-rays, which was in agreement with the experimental results.

1. Introduction

X-rays and γ-rays have been widely used in medical diagnosis, homeland security, nondestructive testing and scientific research [1–3]. Compared with commercial silicon and amorphous selenium (α-Se), lead halide perovskite has a higher attenuation coefficient due to its high atomic number. Halide perovskite have a low defect density and high inhibition of carrier recombination. Due to its performance, the halide perovskite shows a large charge mobility-lifetime product, and a large charge mobility-lifetime product ensures charge collection efficiency under a small electric field and avoids a large dark current [4,5]. The tuneable optical band gap causes the detector to have high energy resolution, large resistivity and low leakage current [6]. In the field of medical diagnosis, the achievement of more accurate early diagnosis of diseases usually needs an increase in the radiation dose; however, a radiation dose that is too high has adverse effects on the human body and even leads to changes in genetic material. Therefore, to improve the detection sensitivity, high atomic number materials are usually used to ensure that the X-ray radiation to the human body is effectively reduced without reducing the diagnostic imaging [7–9]. In recent years, perovskite materials have become the preferred materials for direct X-ray detectors [1,5,10,11,12]. The use of these materials are anticipated to overcome the shortcomings of high cost and low

* Corresponding author.
E-mail address: wujj@nim.ac.cn (J.J. Wu).

https://doi.org/10.1016/j.heliyon.2023.e18875
Received 28 May 2023; Received in revised form 1 August 2023; Accepted 1 August 2023
Available online 1 August 2023

sensitivity of existing semiconductor detectors and achieve the development of X-ray detectors with room temperature operation, high sensitivity and high energy spectrum resolution.

Hou Yu Xin et al. reviewed the development of X-ray detectors from the perspective of the structure and materials of X-ray detectors, discussed the absorption and detection performance of different detection materials for X-rays, and finally prospected the future development direction of X-ray detectors [13]. In 2007, Gui et al. conducted a simulation study of the direct X-ray detectors. EGSnrc was used to simulate the response characteristics of several direct X-ray detectors such as HgI_2 in the medical X-ray range [14]. In 2019, Henning Mescher et al. combined the superior performance of single crystal perovskite materials and the low cost characteristics of polycrystalline conversion layers and simulated the response performance of folded perovskites under different structures and photon energies through model analysis of detection sensitivity and detection quantum efficiency [15]. In 2021, Li et al. used the Monte Carlo method to simulate the external photoelectric effect sensitivity and quantum efficiency of perovskite crystals. On this basis, the influence of crystal thickness on the sensitivity of $CsPbX_3$ was discussed to explore the application prospects of $CsPbX_3$ crystals in the field of X-ray vacuum optoelectronic devices [16]. In 2022, Zhang et al. simulated the spatial resolution of X-ray imaging of a perovskite quantum dot/polymer composite scintillator. At the of energy of 20 keV, its spatial resolution was comparable to that of a commercial CsI scintillator; their study showed that lead halide perovskite has great potential in low energy X-ray medical imaging [17].

In the paper, the response characteristics of the $MAPbBr_3$ perovskite direct conversion X-ray detector were simulated based on the Geant4 Monte Carlo method. From the characteristics of the mass attenuation coefficient, absorption efficiency and detection sensitivity comparing α-Se and CdTe semiconductor materials, the advantages of perovskite materials in the field of radiation detection were demonstrated from multiple perspectives.

2. Principle and method

2.1. Simulated geometric model of the $MAPbBr_3$ detector

Geant4 is a Monte Carlo simulation code developed by the European Organization for Nuclear Research based on the C++ object oriented programming method, which is used to simulate the physical process of particle transport in material [18,19]. Geant4 code was used to simulate the physical process of X-ray interaction with perovskite direct detectors, including the photoelectric effect, Compton effect and electron pair effect. As shown in Fig. 1a, Geant4 could obtain the data information of the energy deposition

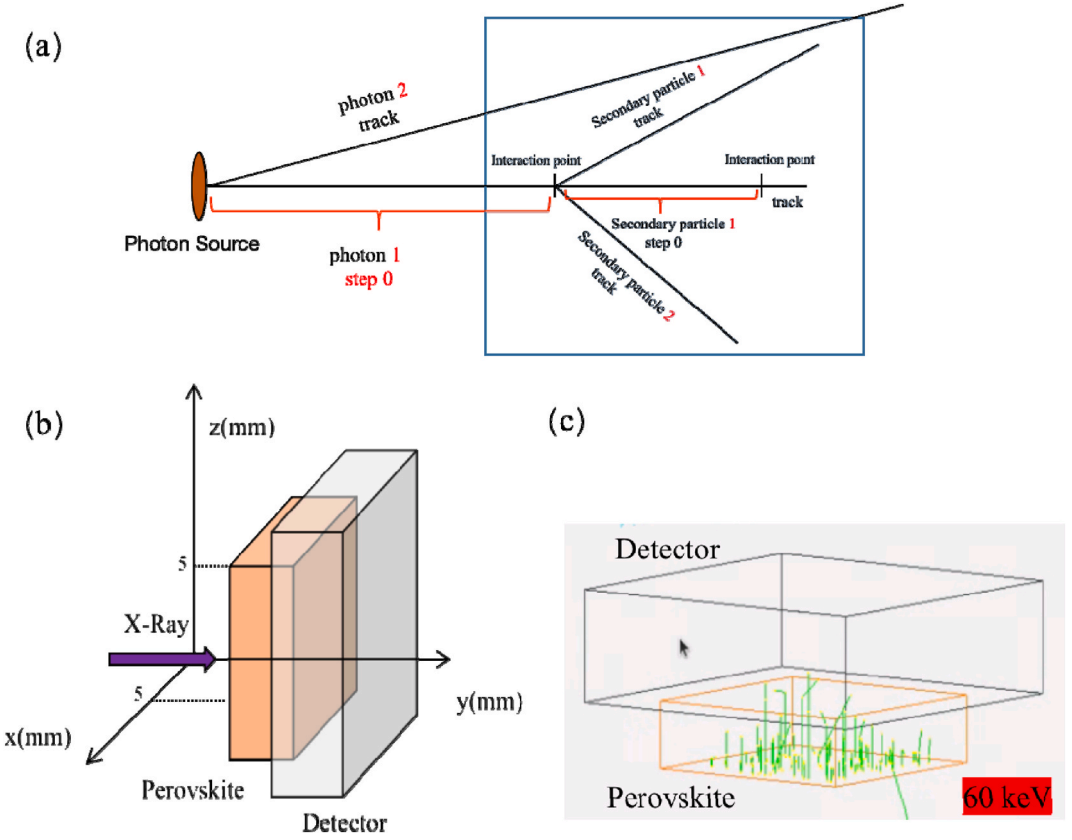

Fig. 1. (a) Single photon life cycle diagram. (b) Structure diagram of the geometric model. (c) Three-dimensional model built by Geant4 simulation.

position and size of each step. In the SteppinActio class, the energy deposited in each step of the crystal was counted and accumulated into an event energy deposition, which represented the energy deposited by a photon from its reaction to the end of its path in the crystal. The total deposition energy, which was the accumulation of energy deposited in each event, was output in the "run". To obtain the required energy spectrum, the total deposited energy needed to be written in the "run" of the root file.

To study the X-ray attenuation ability of the crystal, a geometric model is established, as shown in Fig. 1b. When setting the crystal material in the Detector Construction, the influence of the device fabrication process is not considered, and only the physical parameters of the crystal material are considered. The geometric plane size of the $MAPbBr_3$ crystal is 10 mm × 10 mm, and the y-axis passes through the geometric centre of the model. The thickness is selected from 0 mm to 5 mm, and the density is 3.8 g cm^{-3}. The left side is the position where the crystal is placed. A detector is placed behind the crystal to collect the number of X-rays that pass through the crystal. The size of the detector is 15 mm × 15 mm × 5 mm. The surface area of the detector is larger than that of the crystal, such that the photons could pass through the crystal and be collected by the detector. Fig. 1c shows the geometry of the interaction between the $MAPbBr_3$ crystal and 60 keV X-rays. The particle source is set as a 10^8 monoenergetic γ photon, which is incident in the perovskite in the vertical direction of a 4 mm × 4 mm surface source shape. This position coincides with the left surface of the crystal.

2.2. Photon absorption efficiency and mass attenuation coefficient

For photons with various energies the penetration ability of the material is different. When a beam of photons passes through a semiconductor material with a thickness *d*, the mass attenuation coefficients can be obtained by the transmission method according to Beer Lambert's law in Eq. (1). The photon absorption efficiency of materials can be expressed in Eq. (2) [20,21].

$$I = I_0 e^{-(\mu/\rho)\rho d} \tag{1}$$

$$\eta = 1 - e^{-(\mu/\rho)\rho d} \tag{2}$$

where I_0 and I are the incident and attenuated photon strengths: ρ is the material density; μ is the linear attenuation coefficient and d is the thickness of the material. μ/ρ is the mass attenuation coefficient ($cm^2 \cdot g^{-1}$), which can be obtained from the NIST database.

The mass attenuation coefficient refers to the absorption capacity of the material to the X-ray. It is a physical quantity describing the effect of material density and composition on the absorption capacity of the X-ray. It is only concerned with the energy of radiation and the atomic structure of the material [20].

Geant4 simulates physical processes, such as the photoelectric effect and Compton effect, of perovskite crystal materials with photons of different energies. By recording the number of photons entering the sensitive volume detector, the photon absorption rate and mass attenuation coefficient of the material are calculated.

2.3. Charge collection efficiency

When a photon with an initial energy of E_0 is incident into the material, the inelastic collision with the electrons outside the nucleus causes the medium to be ionized and excited. Due to the loss of energy, electron hole pairs are generated. These processes are random events and obey the Fano distribution. When the particle base is large enough, the expected electron hole pair N_0 can be expressed by the linear relationship in Eq. (3) [22].

$$N_0 = \frac{E}{w} \tag{3}$$

where w is the average ionization energy of the material and indicates the energy required for the material to generate an electron-hole pair; E is the total energy deposited in the material; N_0 is the number of electron-hole pairs produced.

When the interactions between the photons and materials generate electrons and holes, they drift towards the positive and negative electrodes under the action of a bias voltage. Thus, the electrons and holes are collected on the positive and negative plates, respectively. The actual charge collected on the plate is determined by the charge collection efficiency and the number of charges generated by the material. The charge collection efficiency can be calculated by the Hecht equation [23–25]. The charge collection number $\Delta Q_{(y)}$ at any incident depth y can be obtained in Eq. (4). Then, the total charge collection number is obtained by integrating with respect to the thickness direction of the material [25–27].

$$\Delta Q_{(y)} = \frac{N_0 \lambda_e}{d}\left(1 - e^{-(d-y)/\lambda_e}\right) + \frac{N_0 \lambda_h}{d}\left(1 - e^{-y/\lambda_h}\right) \tag{4}$$

Table 1
Parameters of $MAPbBr_3$, α-Se, CdTe crystals.

Material	ρ/g·cm^{-3}	E/V·cm^{-1}	w/eV	$\mu_e\tau_e$/cm^2·V^{-1}	$\mu_h\tau_h$/cm^2·V^{-1}
$MAPbBr_3$ [10]	3.8	20	5.3	2.85×10^{-2}	1.4×10^{-2}
α-Se [28]	4.3	80000	43	10^{-6}	10^{-5}
CdTe [29]	5.85	7000	4.6	10^{-4}	2×10^{-5}

where $\lambda_e = \mu_e \tau_e E$ is the average free path of electrons; $\lambda_h = \mu_h \lambda_h E$ is the average free path of holes; d is the distance between the anode plate and the cathode plate of the detector (cm); E is the electric field intensity in the detector (V·cm^{-1}); and y is the linear distance between the position where the X-ray interacts with the crystal and the negative plate (cm). Typical parameters for the three materials are shown in Table 1.

The charge collection of the electrode is mainly due to the movement of electrons to the anode and holes to the cathode. With increasing incident depth, the distance between the electron and the anode increases, and the transit time of the photogenerated carriers also increases. Thus the probability of electron capture increases, and a decrease in electron collection efficiency is observed. When the distance between the hole and the cathode is shortened, the probability of hole trapping decreases, resulting in an increase in hole collection efficiency. The charge collection efficiency of the $MAPbBr_3$ crystal is mainly contributed by electrons. When the incident depth increases, the downward trend of the electron collection efficiency is stronger, and the upward trend of the hole collection efficiency is slower. This causes the charge collection efficiency to initially increase first and then decrease.

As shown in Fig. 2a, when the electric field is 5 V cm^{-1}, the maximum charge collection efficiency of the $MAPbBr_3$ crystal with a thickness of 2 mm is 64.0%. When the electric field is set to 20 V cm^{-1}, the maximum charge collection efficiency is 88.9%. With increasing electric field intensity, the drift velocity of photogenerated carriers to the electrode becomes faster, and the probability of capture and recombination during drift is reduced. As a result, the charge collection efficiency gradually increases.

Fig. 2b shows the charge collection efficiency of the three crystals under different electric field strengths. When the maximum charge collection efficiency of the $MAPbBr_3$ crystal with a thickness of 2 mm is 88.9%, the electric field intensity is only 20 V cm^{-1}. When the maximum charge collection efficiency of the CdTe crystal is 88.9%, the electric field strength is 7000 V cm^{-1}. When the maximum charge collection efficiency of α-Se is 89.4%, the electric field strength is as high as 80000 V cm^{-1}. However, a greater electric field strength correlates to a greater dark current generated by the device, which directly affects the performance of the detector.

2.4. Detection sensitivity

The detection sensitivity of the direct conversion X-ray detector is an important performance index, which is defined as the number of charges collected per unit radiation dose per unit area in Eq. (5) [15,30,28].

$$S = \frac{Q}{AX} \tag{5}$$

where Q is the amount of charge (C); A is the area (cm^2); X is the radiation dose (Gy); and S is the detection sensitivity (C Gy_{air}^{-1}·cm^{-2}·).

Geant4 is used to count the energy deposition data of each action when photons of different energies are incident on different materials. The average number of signal charges N contributed by each photon energy is calculated. The material information used are shown in Table 1. The number of photons incident per unit area (cm^2) per unit radiation dose (Gy) can be expressed by Φ. The detection sensitivity can be obtained by simulating the product of the number of signal charges generated by each photon and the number of photons Φ at different energies [28,29,31].

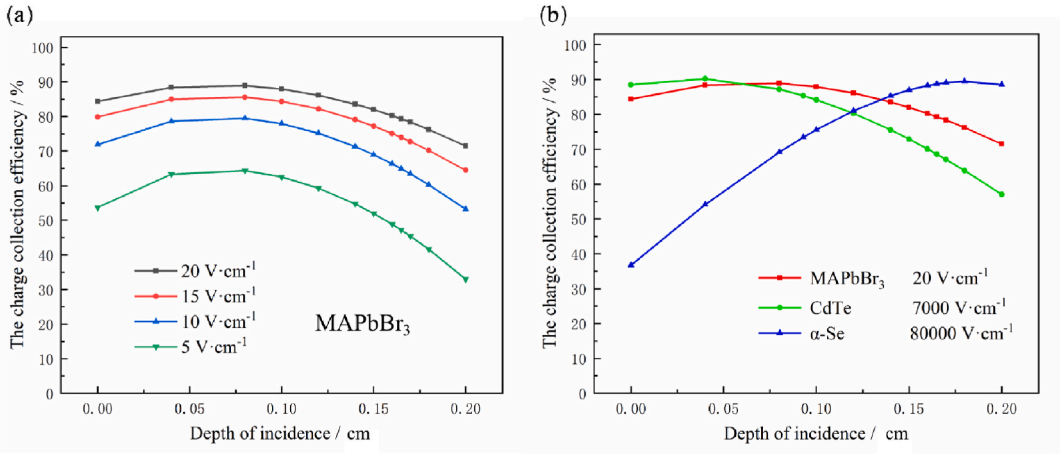

Fig. 2. (a) Calculation of the charge collection efficiency of $MAPbBr_3$ with a thickness of 2 mm under different electric field strengths. **(b)** Calculation of the charge collection efficiency of $MAPbBr_3$, CdTe and α-Se with a thickness of 2 mm under different electric field strengths.

3. Results

3.1. Absorption efficiency

The absorption efficiency is used to evaluate the performance of the detector. High absorption efficiency can reduce the crystal thickness to achieve efficient photon absorption. For energies in the range of 30 keV to 100 keV, Geant4 was used to simulate the absorption efficiency of $MAPbBr_3$, amorphous Se and CdTe with a thickness of 1 mm at different energies. As shown in Fig. 3a, the absorption efficiency generally decreased with increasing X-ray energy, and the absorption efficiency of $MAPbBr_3$ was significantly higher than that of amorphous Se. The absorption efficiency of $MAPbBr_3$ at 88 keV suddenly increased, which was consistent with the K-layer absorption limit of Pb in the mass attenuation coefficient of Fig. 5b. Since the photon absorption efficiency of CdTe with a thickness of 1 mm was close to 100% in the range of 30 keV to 40 keV, the 31.8 keV absorption limit of CdTe is not evident in Fig. 3a. At the same energy, the absorption efficiency of the crystal increased with increasing crystal thickness. For 60 keV X-ray photons, 4 mm thick $MAPbBr_3$ was sufficient to attenuate the incident photons by 99.3%, while 4 mm thick amorphous Se attenuated the incident photons by 97.7%. Due to the large average atomic number of CdTe, its absorption efficiency was significantly higher than that of $MAPbBr_3$, and the absorption rate of CdTe with a 1 mm thickness reached 97.5%.

The absorption efficiency of $MAPbBr_3$ crystals with different thicknesses varies with energy, as shown in Fig. 4a. When the thickness of the $MAPbBr_3$ crystal increases from 1 mm to 5 mm, the absorption efficiency of the crystal with a thickness of 1 mm is as high as 97.6% for photon energies below 40 keV. However, when the energy of the ray is higher than 40 keV, the absorption efficiency of the crystal with a thickness of 1 mm begins to decrease at an extremely fast rate. When the energy is 88 keV, the absorption efficiency of the 1 mm thick crystal is 34.5%. When the energy is higher than 88 keV, the photon energy is deposited inside the crystal because the K layer electrons of Pb are struck by the X-ray, leading to a sudden increase in the absorption efficiency of the crystal to the X-ray. In the case of constant X-ray energy, with an increase in the thickness of the crystal, the detection efficiency shows a significant upward trend.

The comparison of the absorption efficiency of a 1 mm thick $MAPbBr_3$ crystal with or without considering the relaxation process under different photon energies is shown in Fig. 4b. When the energy is lower than 88 keV, the absorption efficiency is basically the same whether the relaxation process is considered. When the energy is higher than 88 keV, the absorption efficiency considering the relaxation process is low. Based on physical process of Geant4 simulating the interaction between X-rays and crystals, when the relaxation process is turned off, all of the energy of the photons are given to the electrons when photoelectric absorption occurs. In the relaxation process, the K layer absorption limit of Pb is reached, and the incident photons interact with the K layer electrons to produce fluorescence emission. Part of the fluorescence escapes from the crystal and causes the absorption efficiency to decrease.

3.2. Mass attenuation coefficient

The mass attenuation coefficients of $MAPbBr_3$, CdTe and amorphous Se in the photon energy range of 1 keV-10^3 MeV are calculated based on the NIST photon cross-section database in Fig. 5a [32]. Regardless of the resonance absorption of the K, L and M edges, the mass attenuation coefficient of $MAPbBr_3$ in the whole energy region is higher than that of amorphous Se and close to that of CdTe.

The mass attenuation coefficient based on the Geant4 simulation is shown in Fig. 5b. The position of the absorption limit of $MAPbBr_3$ at 88 keV effectively coincides with the database. The deviation between the simulation results of $MAPbBr_3$ and the NIST database is within 1.39% in Fig. 5c. The difference in the physical process of the photon-material interaction between the Geant4 program and the NIST database causes this deviation. The results verify the accuracy of the model established using Geant4.

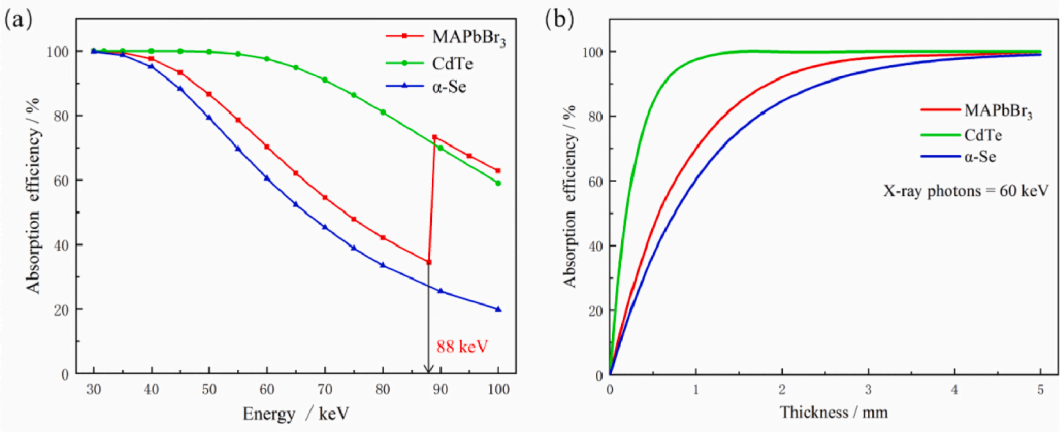

Fig. 3. (a) Absorption efficiency of $MAPbBr_3$, CdTe and amorphous Se with a thickness of 1 mm at different energies. **(b)** Calculation of the X-ray photon absorption efficiencies of $MAPbBr_3$, CdTe and amorphous Se with different thicknesses at 60 keV.

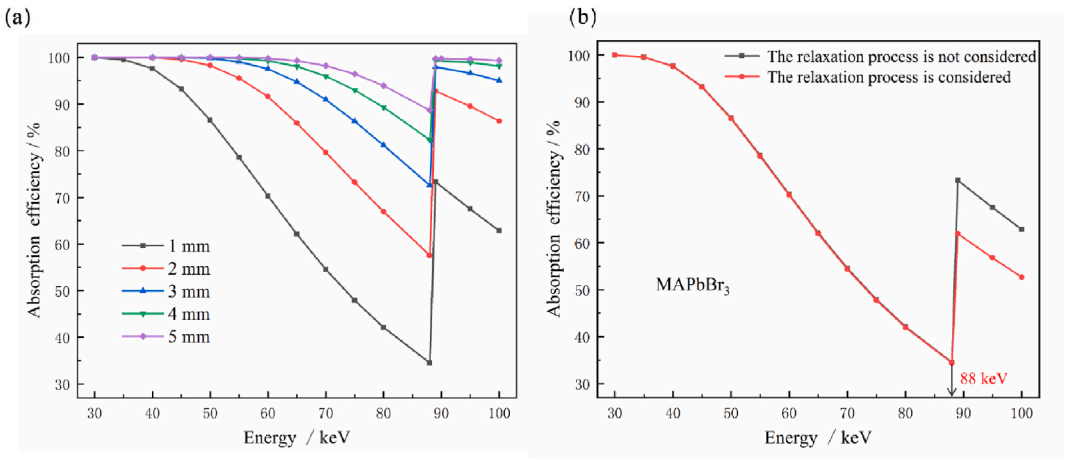

Fig. 4. (a) Simulation of the absorption efficiency of $MAPbBr_3$ crystals with different thicknesses. **(b)** Simulation of the absorption efficiency of $MAPbBr_3$ crystals considering the relaxation process or not under different energies.

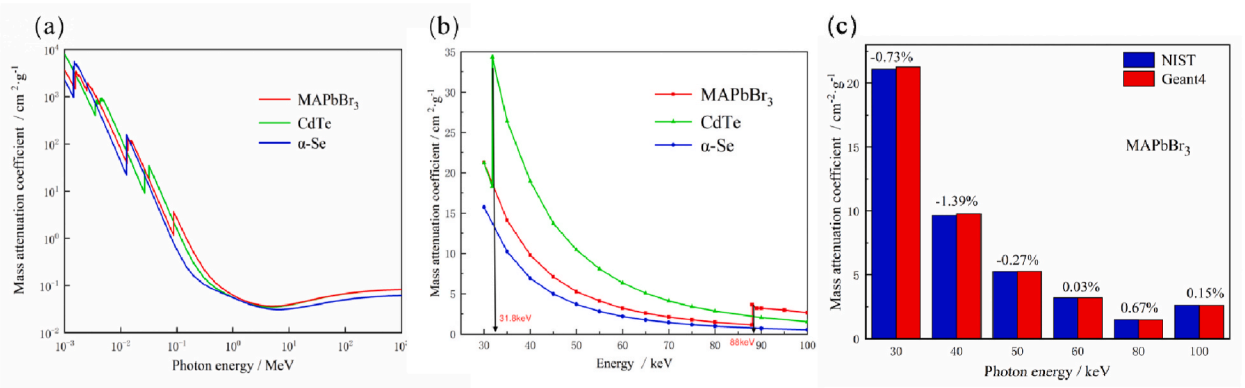

Fig. 5. (a) Mass attenuation coefficients of $MAPbBr_3$, CdTe and amorphous Se provided by the NIST database. **(b)** Simulation of the mass attenuation coefficient in the energy range of 30 keV to 100 keV using Geant4. (c) Comparison of mass attenuation coefficients of $MAPbBr_3$ obtained by Geant4 and the NIST database.

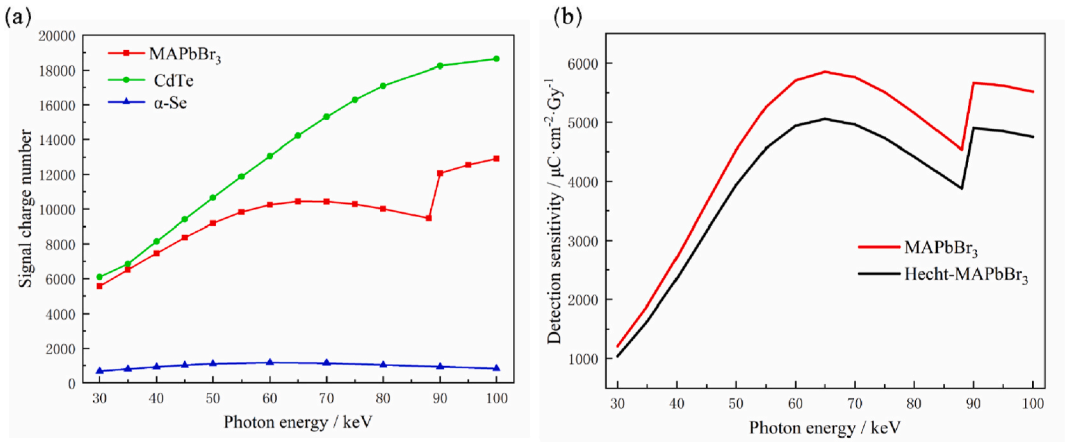

Fig. 6. (a) Number of signal charges collected on the electrode by each photon. **(b)** Calculation of the detection sensitivity of the $MAPbBr_3$ crystal at different photon energies.

3.3. Number of generated charges and detection sensitivity

Due to the presence of impurities and defects, the carriers in the crystal material are trapped, absorb and diffuse during the drift process. Thus, the charge generated by the interaction between the X-rays and crystals is not completely collected by the electrode. For the direct conversion X-ray detectors, the number of signal charges that can be collected on the electrode directly reflect the detection sensitivity of the detector.

The average number of signal charges generated by each photon of the different materials at different energies is shown in Fig. 6a. At the same energy, the number of signal charges produced by the $MAPbBr_3$ crystal and CdTe crystal are much higher than that produced by amorphous Se. Due to the low atomic number of amorphous Se, the absorption rate of X-rays is low. Moreover, the average ionization energy of amorphous Se is 43 eV, which is much higher than that of $MAPbBr_3$ crystals and CdTe crystals. This leads to fewer number of signal charges generated by amorphous Se.

As shown in Fig. 6b, the detection sensitivity of the $MAPbBr_3$ crystal is slightly lower based on a comparison between the charge collection efficiency to the total charge collection. The charge collection efficiency increases with higher applied electric field strength. When the photon energy is higher than 88 keV, the K layer absorption limit of Pb is reached; thus, more energy is deposited by the interaction between the X-ray and $MAPbBr_3$ crystal, resulting in a sharp increase in the number of signal charges generated by the crystal. Therefore, the detection sensitivity of the detector is also increased.

When the photon energy is 60 keV, the detection sensitivity of the different crystals varies with the thickness, as shown in Fig. 7a. When the charge is assumed to be completely collected, the detection sensitivity of the crystals increases with increasing thickness. Finally, a saturated state is obtained. The detection sensitivity of the CdTe crystal is higher than that of the $MAPbBr_3$ crystal. Due to the low charge collection efficiency of CdTe crystals and the excessive applied electric field, the dark current will be too high. As shown in Fig. 7b, when the charge collection efficiency is considered, the detection sensitivity of the $MAPbBr_3$ crystal initially increases and then decreases when the applied electric field is 20 V cm^{-1}. The optimal detection sensitivity is observed at a distance of 2 mm. Since the average free path of the hole ($\mu_h\tau_hE$) in the $MAPbBr_3$ crystal is 2.8 mm, when the crystal thickness is less than 2.8 mm, the energy of X-ray deposition in the crystal increases with the increasing thickness. The increased charge collected between the plates leads to increased detection sensitivity. When the crystal thickness is greater than 2.8 mm, the trap effect leads to more hole loss. The charge collected between the plates is mainly contributed by electrons, which leads to low charge collection efficiency.

$MAPbBr_3$ crystals with a thickness of 2 mm were prepared by the antisolvent method. The device structure is shown in Fig. 8a. We exposed the $MAPbBr_3$ single-crystal device to a X-ray source with X-ray effective energies of 39 keV, 60 keV and 80 keV, for which the radiation dose rate was calibrated. As shown in Fig. 3b, the 2 mm thick $MAPbBr_3$ could almost completely absorb the X-rays within the energy range of the X-ray source used. The absorption contribution of the very thin silver electrode to X-rays was negligible. By turning on and off the incident X-ray, the photocurrent intensity was measured to confirm the response of the single crystal device to X-rays.

The total dose rate of the X-ray beam is controlled by changing the tube current of the X-ray tube. As shown in Fig. 8b, the radiation detector exhibits a much higher detection sensitivity when exposed to X-ray energy with an effective energy of 60 keV compared to when exposed to 39 keV and 80 keV energy. Without considering the influence of the device fabrication process, this phenomenon is consistent with the simulation results shown in Fig. 6b. As shown in Fig. 8c, the sensitivity of the radiation detector for detection proportionally increases with the increase in applied bias voltage. The collection efficiency of the photogenerated carriers in the detector is improved by increasing the bias voltage, which enhances the detection sensitivity of the radiation detector. Therefore, an effective method to improve detection sensitivity is by increasing the bias voltage of the device.

4. Conclusions

The lead halide perovskite $MAPbBr_3$ is a semiconductor material with a high atomic number and high attenuation coefficient. It has the characteristics of low defect density, low dark current and high charge mobility-lifetime product and shows great potential in the field of ionizing radiation detection. The results of the absorption efficiency and mass attenuation coefficient of perovskite crystals in the energy range of 30 keV to 100 keV for X-rays based on Monte Carlo simulation are provided. For the mass attenuation coefficients, the deviations were within 1.39% compared with the NIST database results. The simulation was able to calculate the signal charge and detection sensitivity of the $MAPbBr_3$ crystal. The results showed that the average free path of the charge carriers will significantly affect the detection sensitivity, indicating the necessity to improve the material's charge carrier mobility-lifetime product. The detection sensitivity of $MAPbBr_3$ crystals was more than nine times that of amorphous Se. The detection sensitivity of CdTe crystals was higher than that of $MAPbBr_3$ crystals, but the low charge carrier mobility-lifetime product of CdTe crystals was smaller. To improve the charge collection efficiency, the electric field needed to be increased. However, a high dark current would form and the device performance would be affected. In summary, materials with high atomic number and high charge carrier mobility-lifetime products, such as $MAPbBr_3$ crystals, could improve the detection sensitivity of medical X-rays. Therefore, the radiation dose to the human body would be reduced. Our results could aid in the development of future high performance X-ray imaging equipment.

Author contribution statement

Feng Qin: Conceived and designed the experiments; Performed the experiments; Analyzed and interpreted the data; Wrote the paper.

Rui Zhao: Performed the experiments; Analyzed and interpreted the data.

Wei Feng Zhu: Analyzed and interpreted the data.

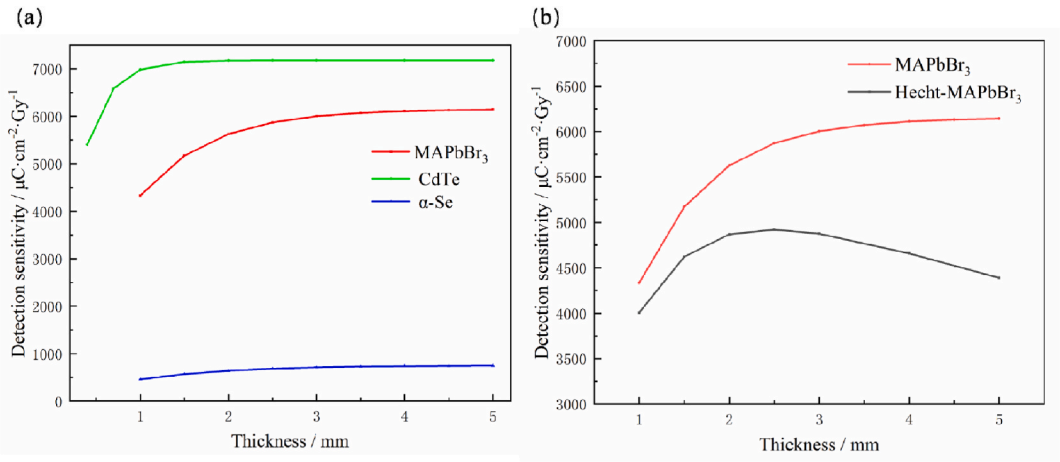

Fig. 7. (a) Variation of the detection sensitivity of each crystal with the thickness at an energy of 60 keV. (b) Change in $MAPbBr_3$ sensitivity with thickness after considering the charge collection efficiency.

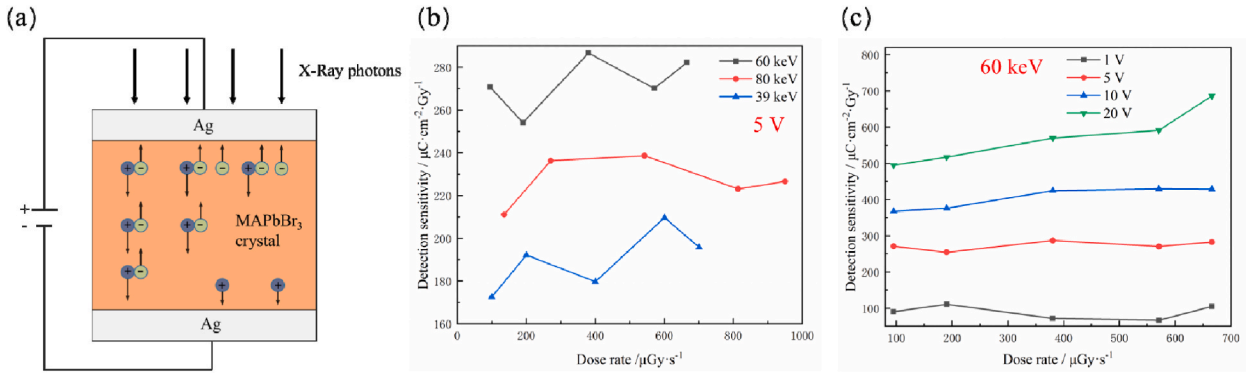

Fig. 8. (a) $MAPbBr_3$ single crystal radiation detector structure. (b) Relationship between the sensitivity of the device and the X-ray radiation dose rate under different X-ray energies. (c) Relationship between the sensitivity of the device and the X-ray radiation dose rate under different bias voltages.

Ning Qin Deng and Zhi Wei Jiao: Contributed reagents, materials, analysis tools or data.
Xian Qiang Tang: Performed the experiments.
Jin Jie Wu: Conceived and designed the experiments.

Data availability statement

Data will be made available on request.

Declaration of competing interest

The authors declare that they have no known competing financial interests or personal relationships that could have appeared to influence the work reported in this paper.

Acknowledgments

This work has been supported in part by the project of National Institute of Metrology China under, Grant AKYZD2311, Grant AKYCX2201, in part by Natural Science Foundation of Beijing under Grant M22020.

References

[1] X. He, Y. Deng, D. Ouyang, et al., Recent development of halide perovskite materials and devices for ionizing radiation detection, Chem. Rev. 123 (4) (2023) 1207–1261.

[2] M.J. Yaffe, J.A. Rowlands, X-ray detectors for digital radiography, Phys. Med. Biol. 42 (1997) 1–39.
[3] M. Tegze, G. Faigel, X-ray holography with atomic resolution, Nature 380 (1996) 49–51.
[4] D.N. Jeong, J.M. Yang, N.G. Park, Roadmap on halide perovskite and related devices, Nanotechnology 31 (2020), 152001.
[5] Q. Hu, Z. Deng, M. Hu, et al., X-ray scintillation in lead-free double perovskite crystals, Sci. China Chem. 61 (2018) 1581–1586.
[6] L. Gao, Q.F. Yan, Recent advances in lead halide perovskites for radiation detectors, Solar Rrl 4 (2) (2020), 1900210.
[7] K.S. Shah, et al., X-ray imaging with PbI_2-based α-Si:H flflat panel detectors, Nucl. Instrum. Methods Phys. Res. A. 458 (2001) 140–147.
[8] S.O. Kasap, et al., X-ray sensitivity of photoconductors: application to stabilized α-Se, J. Phys. D. 33 (2000) 2853.
[9] D.J. Brenner, et al., Estimated risks of radiation induced fatal cancer from pediatric CT, Am. J. Roentgenol. 176 (2001) 289–296.
[10] H. Wei, Y. Fang, P. Mulligan, et al., Sensitive X-ray detectors made of methylammonium lead tribromide perovskite single crystals, Nat. Photonics 10 (2016) 333–339.
[11] S. Yakunin, M. Sytnyk, D. Kriegner, et al., Detection of X-ray photons by solution-processed lead halide perovskites, Nat. Photonics 9 (7) (2015) 444–449.
[12] Y. Liu, X. Zheng, Y. Fang, et al., Ligand assisted growth of perovskite single crystals with low defect density, Nat. Commun. 12 (1) (2021) 1686.
[13] Y.X. Hou, et al., Present status and prospects of X-ray detectors, Physics 50 (8) (2021) 526–533.
[14] J.B. Gui, et al., Use of Monte Carlo method to evaluate the response of direct conversion X-ray detectors, High Energy Phys. Nucl. Phys. 10 (2007) 933–937.
[15] H. Mescher, E. Hamann, U. Lemmer, Simulation and design of folded perovskite x-ray detectors, Sci. Rep. 9 (1) (2019) 5231.
[16] Y.K. Li, et al., External photoelectric effect of $CsPbX_3$ perovskite in X-ray region, Acta Phys. Sin. 70 (19) (2021) 221–227.
[17] Y.Y. Zhang, et al., Simulation of X-ray imaging property of halide lead perovskite scintillators, Nucl. Tech. 45 (12) (2022) 27–34.
[18] S. Agostinelli, J. Allison, K. Amako, et al., GEANT4-a simulation toolkit, Nucl. Instrum. Methods Phys. Res. Sect. A Accel. Spectrom. Detect. Assoc. Equip. 506 (3) (2003) 250–303.
[19] Z.Q. Chen, J.J. Chen, S.B. Shu, et al., Simulation study on the factors affecting the detection efficiency of a $LaBr_3$(Ce) detector, Nucl. Tech. 45 (1) (2022) 58–64.
[20] M.E. Medhat, Y. Wang, Geant4 code for simulation attenuation of gamma rays through scintillation detectors, Ann. Nucl. Energy 62 (2013) 316–320.
[21] T.B. Yang, M. Wang, et al., Efficiency calibration of lanthanum bromide scintillation detector and analysis of influencing factors of the detection efficiency, Nucl. Tech. 44 (10) (2021) 25–31.
[22] A. Ruzin, Y. Nemirovsky, Statistical models for charge collection efficiency and variance in semiconductor spectrometers, J. Appl. Phys. 82 (6) (1997) 2754–2758.
[23] M.Z. Kabir, Effects of charge carrier trapping on polycrystalline PbO X-ray imaging detectors, J. Appl. Phys. 104 (7) (2008), 074506.
[24] M.Z. Kabir, E.V. Emelianova, V.I. Arkhipov, et al., The effects of large signals on charge collection in radiation detectors: application to amorphous selenium detectors, J. Appl. Phys. 99 (12) (2006), 124501.
[25] H.Z. Zhou, et al., Simulating response to gamma ray of CdZnTe detector with CAPture electrode using Geant4, Atomic Energy Sci. Technol. 55 (6) (2021) 1098–1104.
[26] D.M. Panneerselvam, M.Z. Kabir, et al., Evaluation of organic perovskite photoconductors for direct conversion X-ray imaging detectors, J. Mater. Sci. Mater. Electron. 28 (2017) 7083–7090.
[27] A. Ruzin, Y. Nemirovsky, et al., Methodology for evaluation of mobility-lifetime product by spectroscopy measurements in CdZnTe spectrometers, J. Appl. Phys. 82 (9) (1997) 4166–4171.
[28] S.O. Kasap, X-ray sensitivity of photoconductors: application to stabilized α-Se, J. Phys. Appl. Phys. 33 (21) (2000) 2853.
[29] S.A. Kolosov, Y.V. Klevkov, A.F. Plotnikov, et al., Electrical properties of fine-grained polycrystalline CdTe, Semiconductors 38 (2004) 455–460.
[30] H. Zhang, G. Dun, Q. Feng, et al., Encapsulated X-ray detector enabled by all-inorganic lead-free perovskite film with high sensitivity and low detection limit, IEEE Trans. Electron. Dev. 67 (8) (2020) 3191–3198.
[31] S. Siddiquee, M.Z. Kabir, et al., Modeling of photocurrent and lag signals in amorphous selenium x-ray detectors, J. Vac. Sci. Technol. A: Vac. Surf. Films 33 (4) (2015), 041514.
[32] M.J. Berger, Photon Cross Sections Database. NIST Standard Reference Database 8 (XGAM), 1998. http://physics.nist.Gov/PhysRefData/Xcom/Text/XCOM.